Extreme block and boulder transport along a cliffed coastline (Calicoan Island, Philippines) during Super Typhoon Haiyan

AUTHOR(S):

Kennedy, Andrew B.; Mori, Nobuhito; Yasuda, Tomohiro; Shimozono, Takenori; Tomiczek, Tori; Donahue, Aaron; Shimura, Tomoya; Imai, Yuki

CITATION:

Kennedy, Andrew B. ...[et al]. Extreme block and boulder transport along a cliffed coastline (Calicoan Island, Philippines) during Super Typhoon Haiyan. Marine Geology 2017, 383: 65-77

ISSUE DATE:

2017-01-01

URL:

http://hdl.handle.net/2433/219509

Extreme Block and Boulder Transport along a Cliffed Coastline during Super Typhoon Haiyan

Andrew B. Kennedy[1], Nobuhito Mori[2], Tomohiro Yasuda[2], Takenori Shimozono[3], Tori Tomiczek[1], Aaron Donahue[1], Tomoya Shimura[2], and Yuki Imai[2]

[1] Department of Civil & Environmental Engineering & Earth Sciences, University of Notre Dame, Notre Dame, IN USA.
[2] Disaster Prevention Research Institute, Kyoto University, Uji, Kyoto, Japan.
[3] Department of Civil Engineering, University of Tokyo, Tokyo, Japan.

Abstract

This paper presents data on block and boulder transport during Super Typhoon Haiyan along a 4.5km long, low (5-12m) cliffed coastline in Calicoan Island, Eastern Samar, Philippines. Wave runup exceeding 15.2m elevation drove thousands of limestone clasts, many of which – with volumes up to ~83m^3 – strongly exceed maximum values stated in the literature to be possible from storms, up to ~280m inland. A few very large clasts (65-132m^3) were not transported by the waves. As a group, and along with transport reported in May et al. [2015] at a different location during Haiyan, these appear to be the largest blocks verified to have been transported by storm waves, and suggest that a re-evaluation of storm wave transport capability is necessary. Comparison of present results with a global database of storm boulder transport shows a mass-elevation envelope below which transport is observed and above which no transport observations exist.

Extension of initiation of motion criteria to include non-rectangular cross-sections significantly reduced inferred velocities necessary for boulder transport during Haiyan, particularly for overturning boulders. Still, the potential range of velocities remained significant once coefficient uncertainty was considered. Lifting/joint-bounded velocity estimates at cliff edges were much larger than for other transport modes, and are difficult to reconcile: it is suggested that processes at cliff edges may be significantly more complex than can be accurately represented with these simple theories.

1. Introduction

1.1 Block and Boulder Transport During Large Inundation Events

Coastal block (secondary axis b>4096mm) and boulder (256mm<b<4096mm) transport has been recorded many times during historical storms and tsunamis [e.g. Goto et al., 2011; Paris et al., 2011; Nandasena et al., 2013; May et al., 2015]. Because large rocks are both durable and easily visible, these clasts are often used as markers to identify the existence and estimate the magnitude of inundation events in the absence of other records (e,g, Imamura et al., 2008). Both

existence and magnitude are important for present day planning: evidence from specific sites is valuable for risk evaluation and management, while more general links between hydrodynamics, forces, and transport are useful in predicting conditions that may be experienced at other locations.

Transport from tropical cyclone waves, which is the focus of this paper, has been reported for one tonne (t) boulders on 20m clifftops in the Okinawan Islands [Goto et al., 2011], and for far larger boulders (for simplicity we omit “block” from most text) at lower altitudes in many other locations [e.g., Khan et al., 2010; May et al., 2015], while strong winter storms have emplaced boulders at high elevations in the Aran Islands, Ireland [Williams and Hall, 2004; Cox et al., 2012], Banneg Island, France [Fichaut and Suanez, 2011], and Enderby Island [McFadgen and Yaldwyn, 1984]. At higher elevations, which will be the focus of this paper, storm wave transport can generate overland features that include ridges (Hall et al., 2008), boulder beaches (Etienne and Paris, 2010), and isolated or scattered boulders (Khan et al., 2010; Goto et al., 2011). Unsurprisingly, locations with larger waves show transport of larger boulders, and to higher elevations. However, although there has been considerable progress made in storm wave transport, it is safe to say that the accurate inference of storm characteristics from boulder deposits is not yet a solved problem.

Boulder transport has been widely used to infer tsunami inundation in Japan (Hisamitu et al.,2014), Aruba (Scheffers et al., 2005), Iran (Shah-hosseini et al., 2011), Italy (Mastronuzzi et al., 2007) and many other locations. These studies tend to use initiation of motion criteria combined with assumptions about tsunami Froude numbers (Nott, 2003; Nandasena et al., 2011), although numerical models have been used in some instances (Imamura et al., 2008). Direct observations of boulder transport by tsunamis exist for numerous recent historical events [Paris et al., 2009; Bourgeois and MacInnes, 2010; Nandasena et al., 2013] where the magnitude of the tsunami is better known. There is a clear division in size between the largest tsunami boulders [e.g. Frolich et al., 2009; Ramalho et al., 2015] and those emplaced by known storm waves [May et al., 2015], but there is considerable overlap over the observed range.

While distinction between storm and tsunami transport is straightforward in some instances, it is not always obvious. Parametric force and moment balances [e.g. Nandasena et al., 2011] are often used for both storms and tsunamis to estimate velocities at incipient motion for different transport modes such as overturning, sliding or lifting/saltation. A major assumption is usually then made where storm waves have a local Froude number of unity, while tsunamis have Froude numbers of two. This leads directly to the assumption that storm waves must be four times larger than tsunamis to transport the same size boulders (Nott, 2003). This large discrepancy often leads to inferred storm wave heights that are unrealistically large while tsunami heights are much smaller and more reasonable (e.g. Kelletat et al., 2004). However, although widely used, incipient motion relations and the assumptions they are based on have received very little validation; i.e. velocity and height inferences have not been independently confirmed. Thus, there remains an active debate over the origins of some boulder fields and the methods used to estimate event magnitudes – these disputes may be partially resolved from analysis and intercomparison of transport during both storm and tsunami mega-events. In this paper we present observations of block and boulder transport during Typhoon Haiyan. Results are used to help define the envelope of transport space during extreme storms, and to evaluate and improve widely-used techniques for inferring event fluid velocities.

1.2 Super Typhoon Haiyan

With estimated one minute sustained winds of 170 knots (87m/s), Super Typhoon Haiyan may have been the strongest landfalling tropical cyclone of the satellite era when it passed the Philippine islands of Samar and Leyte on November 7, 2013 (Fig. 1a) [Joint Typhoon Warning Center, 2013]. Areas near landfall suffered catastrophic damage, with more than 6,000 fatalities and greater than one million buildings damaged or destroyed. [National Disaster Risk Reduction and Management Council, 2014]. Largest storm surge values were found in shallow San Pedro Bay near the city of Tacloban, with surge to 5-6m, and runup to 7-8m [Tajima et al., 2014, Mas et al., 2015]. In contrast, the open Pacific coast near the present study region had predicted offshore surge of less than 0.3m because bathymetry drops steeply into the Philippine Trench [Mori et al., 2014]. However, Figure 1a shows extreme waves during Haiyan, with a hindcast peak significant wave height of H_s=18.7m just offshore of the study region [Mori et al., 2014].

The site itself, as shown in Figures 1b and 2a, is a region of low limestone cliffs (5-12m cliff elevations from mean sea level, MSL) north of Ngolos Beach on Calicoan Island. The cliffs are from the Upper Pliocene-Pleistocene Calicoan Limestone formation, which extends north from Calicoan Island with outcrops along the eastern coast of Samar. The rock is a "reef facies limestone built as distinct reefs along the coast by mollusks and algae", with "corals, shells, and algae structures" very evident (Travaglia et al., 1978). Study region bedrock topography seen in Figure 2b shows heavy karst weathering with typical vertical roughness of 0.5-1m, and with extremely sharp phytokarst pinnacles in the sea-spray region (Taborosi and Kazmer, 2013). Large caves and other karst features are found nearby. Some sections of coastal cliffs are fronted by horizontal shore platforms with around 1-2m elevation MSL and width ~20m, while other sections have vertical or overhanging cliffs with no platforms. In non-storm conditions, waves impacting on these cliffs generate vertical jets extending well over 10m into the air (Supporting Video S1). During Haiyan, runup overtopped all coastal cliffs in the study region. While beaches north and south of these cliffs are fronted by fringing reefs several hundred meters wide as seen in Fig. 1b, no reefs are found in front of the cliffs (Fig. 2a). Away from the immediate cliff faces, elevations increase gradually to much larger hills and cliffs 100-400 meters inland. Figure 1c shows some partial transects taken through the boulder transport region.

Runup was extreme during Haiyan, with nearby magnitudes measured up to 14.1m above sea level [Tajima et al., 2014; Shimozono et al., 2015; Roeber and Bricker, 2015]. Satellite-visible vegetation loss and soil erosion were observed for several hundred meters inland, often with prominent terminal debris clusters often composed of logs, sometimes interspersed with limestone boulders. The extreme runup dislodged and transported inland large numbers of these boulders, many of which were large enough to be clearly visible on satellite photographs.

2. Inundation and Boulder Transport on Calicoan Island Cliffs

Boulders in the 4.5km study region (Fig. 1b, 2a) on Calicoan Island were studied during eight days of ground-level and aerial reconnaissance in January and November, 2015; and using pre- and post-storm satellite images. Large boulder transport during Haiyan has previously been reported by May et al. [2015] onshore of a wide fringing reef approximately 40km north of the

present site. Boulder masses were estimated at up to 180t at sea level, with smaller boulders transported at higher elevation. Kennedy et al. [2016] examined and modeled runup and smaller boulder transport immediately south of the present study region over a smoother beach topography, and found a strongly nonlinear dependence of transport elevations and inland distances on incident wave height. The present study largely differs from these two previous works in that it focuses on transport in a higher elevation cliff region without fringing reefs. Sea level boulders in pocket beaches along the cliffed coastline, some of which were quite large (Fig. 3), were neglected in this survey in favor of higher elevation transport.

As shown in Fig. 4, the study site contains many Haiyan-transported boulders and blocks with characteristic lengths >1m, with totals likely in the low thousands. Exact numbers could not be determined both because of the large number of clasts and because of vegetation regrowth which often required trail-cutting to find and reach individual boulders. Figure 6 gives examples of some of the boulders observed here, while Table 1 presents data on the largest boulders measured here directly. Supplemental Figures S.1.1-S.1.15 give aerial and ground level snapshots for boulders in Table 1. Most large boulders were very angular to subangular, often with different faces showing highly different weathering and angularity (Fig. 7). Although most faces showed high angularity arising from recent breakage and erosional karst weathering, lower faces (pre-storm) on boulders that had already been detached from bedrock tended to be much more rounded. Although all clasts were limestone, colors varied significantly and gave indications of processes and locations. Dark gray upper faces indicated an exposure to both direct sea spray and sunlight, while lighter gray showed a more inland origin. White faces indicated rock that was not directly exposed to the sun. Transported boulders typically had moderate to low sphericity. In many ways, these properties are typical for coastal karst landscapes in humid tropical regions (Taborisi and Kazmer, 2013).

All observed clasts of boulder size or greater appeared to originate subaerially from either the cliff edge or the bedrock somewhat inland. Some boulders had clearly been generated in earlier inundation events and were moved further landward by Haiyan, while others were freshly detached from the bedrock. Karst processes including flowstone and small solution columns

showed some existing boulders' pre-storm locations on bedrock (Fig. 8). Fresh scars showed other locations where new boulders had been generated (Fig 9). However, except in a few cases (boulders 999, N0, N2), it proved impossible to match final and initial locations conclusively. Validating motion during Haiyan was made difficult by the complete vegetative cover pre-storm, rendering it impossible to see boulder locations on satellite images. However, in many cases the presence of perishable debris such as plant material underneath boulders gave conclusive proof of transport, as did signs of overturning/rolling, including new orientations of originally downward facing sides, and impact scars. The color and weathering of bedrock underneath a boulder gave additional evidence of motion in some cases.

Cobble-sized clasts were commonly observed: a small fraction (probably less than 1%) were rounded to well-rounded, suggesting a subaqueous origin (Fig. 10), but no detailed statistics were taken. Almost no sand was observed on this rocky landscape, likely from a lack of source material and in direct contrast to the sandy inland deposits observed immediately to the south [Kennedy et al., 2016]. Inland runup limits shown in Figure 4 were estimated using trimlines and debris lines visible on both standard Google Earth imagery and commercially available 0.5m true color satellite images of the study area, with oblique aerial images used to verify features. These same tools were used to identify locations and approximate sizes of some of the larger boulders, but could not provide a complete picture. More accurate ground-level reconnaissance thus concentrated on some of the largest boulders observed in satellite images and the regions around them.

Boulder principal axis lengths (a,b,c), locations, and elevations above mean sea level were measured directly from ground-level observations using measuring tapes and kinematic GPS (n=76), or (a,b) and locations were estimated from satellite observations (n=379). The satellite observations could reliably detect only larger boulders that differed in color from the surrounding bedrock, and were not covered in debris or hidden by vegetation. Based on ground level observations, satellites provided a severe undercount of boulder quantities, and numbers of intermediate-sized boulders ($a<2.5$m) are many times greater than suggested by satellite observations. Larger boulders were also undercounted, but by a lesser margin. Direct ground

191 measurements given in Table 1 for the largest boulders show 8 storm-transported boulders with
192 a>7m (maximum a=7.7m) and 10 boulders with masses exceeding 100t (maximum 208t). Figure
193 4 shows locations and axis lengths both for directly measured boulders, and for those with sizes
194 estimated from satellite observations (though these are without confirmation of transport during
195 Haiyan). Hundreds of boulders were observed by satellite throughout the study area at up to
196 280m from the shoreline, with on-ground confirmation to estimated inland runup limits.
197 Spatially, boulders did not form the large ridges found on some locations in Ireland or the
198 Caribbean [Williams and Hall, 2004; Watt et al., 2010] which are a signature of storm deposits
199 [Paris et al., 2011], although clustering is evident. As seen in Fig. 11, observed debris clusters
200 were often composed of floating vegetation with boulders sometimes interspersed, while others
201 were primarily rocky. The lack of coherent ridges suggests that inundation events with
202 magnitudes comparable to Haiyan are relatively rare; alternatively, existing ridges may have
203 been destroyed during Haiyan. Beaches composed of smaller boulders and cobbles were found
204 well inland in numerous locations (Fig. 10), suggesting that these were in the swash zone during
205 Haiyan.

206

207 Elevations from MSL were measured at the highest point of many transported boulders, as it was
208 assumed that minimum inundation heights reached at least to this level. Results presented in
209 Table 1 are remarkably consistent, with 14 boulders showing minimum inundation levels of 14m
210 above MSL, and a maximum measured boulder top elevation of 15.2m very near to a vegetative
211 debris cluster with almost identical height. Other measured debris elevations tended to be lower,
212 as vegetative debris would need to be very tall to reach boulder crests. Measured inundation here
213 exceeds the maximum value of 14.1m during Haiyan given in Shimozono et al. [2015] taken less
214 than 20km from the study site. As boulder transport likely requires inundation significantly
215 deeper than the boulder top surface, it is probable that runup elevations exceeded even the 15.2m
216 shown here, but this cannot be proved.

217

218 Of large boulders visible on satellites and subsequently visited during ground level observations,
219 only two showed no evidence of motion (Fig. 12). These were seen on satellites and in aerial
220 imagery to have grey (phytokarst) upper faces, indicating that they had not rolled, and their

motion was considered uncertain prior to ground-level reconnaissance. Both were very large with (a,b,c)= (7.5,6.5,4.5)m, (8.0,5.0,2.7)m (Table 1), and may be formed-in-place tower karst features [Mylroie, 2007; Ford and Williams, 2007] rather than boulders moved by storms or tsunamis. However, this is not certain and it is quite possible that they were generated by an inundation event more powerful than Haiyan. Two other smaller boulders measured during ground reconnaissance were believed to not have moved, with both showing pre-storm root systems and partial burial.

Boulders here seen in satellite photos up to the estimated runup limit have been visually confirmed in some (but not all) cases. Since the visible runup limit extends to almost 300m inland in some portions of the present study, inland distances of boulder transport and runup are much further than is possible from a single wave. In this case, infragravity runup as demonstrated by Shimozono et al. (2015), Roeber and Bricker (2015), and Kennedy et al. (2016) appears to be the likely mechanism. The present low cliff topographies are significantly different from these other locations where infragravity runup has been noted, but still water storm surge was much too low to account for inundation (Mori et al., 2014) and transport and other explanations do not appear to satisfy the observed features. However, until experiments or computations are performed on low cliff topographies such as are found here, details are to some degree speculative.

Frequently, the ability of storm waves to transport large boulders has been discounted when compared to tsunamis. Numerous publications [Benner et al., 2010; Scheffers and Kinis, 2014; Erdmann et al., 2015] have suggested that boulders with volumes greater than ~20m^3 (sometimes reported as 20 tonnes) could not be significantly transported by storm waves. These volumes are greatly exceeded by present results. Using conservative (low) estimates of volume as $V = 0.6abc$ [Engel and May, 2012; May et al., 2015], ground-level observations yield 22 boulders with volumes greater than 20 m^3 and two large boulders with estimated volumes of 83m^3 each. (May et al., 2015 also report volumes up to 75m^3.) Thus, it appears that the envelope of block sizes transportable by storm waves can be extended to at least 80m^3: because a

relatively small portion of the post-Haiyan coastline has been surveyed for boulder transport, this limit cannot be stated as definitive.

Maximum boulder quantities here (a=7.7m, mass~208t, runup>15m) are highly comparable to boulders reported to have been transported by the 2011 Tohoku earthquake tsunami (a=6.5m, mass~140t, ~18m local runup) [Nandasena et al., 2013]; in the 2006 Kuril Islands tsunami (a=3m, mass~37.5t, ~15m runup) [Bourgeois and MacInnes, 2010], and in Sumatra during the 2004 Indian Ocean tsunami (a=7.2m, mass~85t, ~20m local runup) [Paris et al., 2009]. However, maximum boulder dimensions here are less than those inferred from megatsunamis in Ishigaki Island, Japan (a=12.4m, mass>500t, runup ~30m) [Imamura et al, 2008; Hisamatsu et al., 2014], Tonga (a=15m, mass~1600t, runup>20m) [Frohlich et al., 2009]; and Santiago Island, Cape Verde (mass ~700t, runup ~220m) [Ramalho et al., 2015].

3. Present Observations in Global Context

To provide a broader picture of storm boulder transport, masses and elevations from the present study were combined with other literature values as shown in Figure 13, with details in Supplementary Material. Here, we only plot locations with reported storm transport, and a few locations with uncertain transport: sites with inferred or observed tsunami transport are not included. A clear envelope can be seen, with boulder transport possible below certain elevations at a given mass, and no transport observed above. Unsurprisingly, maximum boulder masses decrease strongly with increasing elevations. The upper limits of the envelope are dominated by very large waves from winter storms [McFadgen and Yaldwyn, 1984; Williams and Hall, 2004; Hansom et al., 2008; Etienne and Paris, 2010; Fichaut and Suanez, 2011], and from regions with strong tropical cyclones [Goto et al., 2011; Khan et al., 2010; May et al., 2015; present study]. All of these regions have extreme waves, with maximum potential significant wave heights likely to be in the range Hs=15-20m.

To demonstrate the usefulness of a such an envelope, three locations with some uncertainties in boulder transport were plotted along with the known storm transport: Jones et al. [1992] from

Grand Cayman Island, Nakamura et al. [2014] from Lanyu Island, Taiwan, and Hearty [1997] from Eleuthera Island, Bahamas. All three locations are subject to extreme tropical cyclones but transport has not been definitively distinguished between tsunamis and storms. The megaclasts of Hearty [1997] have the additional complication of being reported to be formed-in-place features and not wave-transported at all [Mylroie, 2007], although this is strongly disputed [Hansen et al., 2016]. Both the Taiwan and Cayman data fall very easily within the range of observed storm transport, which does not guarantee that boulders were transported by storms, but adds additional evidence to support the possibility of storm transport. The Eleuthera data plots quite differently. Here, boulders (with sea levels corrected to the geological period from which they are said to have been generated) have, with a few exceptions, masses much larger than anything observed to have been transported by storm waves. If these were storm transport, either site conditions were absolutely ideal to allow such large clasts to be transported, or storm waves were much larger than modern observations. The larger waves hypothesis has been put forth by Hansen et al. [2016], who argued that climatic conditions caused storms in the late-Eemian to have waves larger than are found even in the strongest tropical cyclones today; however, none of this can yet be considered definitive.

This analysis is not complete. Local setting and inland distance, the presence or absence or reefs, boulder shape, and many other properties will have significant influence on whether transport occurs. However, the most obvious omission here is that all boulder data are plotted together even though wave forcing differs between sites. Thus, the envelope arises entirely from sites with the strongest wave forcing: for sites with weaker wave forcing, it is not clear what form the envelope would take. A more general analysis would nondimensionalize all data by wave heights, boulder shape, rock density and other factors to give results that could be compared across the wave height and boulder size range. This would allow observed boulder transport for large boulders in high waves to be scaled to predict small boulder transport in small waves, and vice-versa. However, this type of analysis would require measured or hindcast wave heights either for specific storms known to cause transport, or for storm climatology at a given site. Such a hindcast is an extremely computationally-intensive undertaking, but is just now of the cusp of what is possible. The authors are in beginning stages of such hindcasts and will report on them as results become available.

4. Initiation of Motion for Observed Boulders

Initiation of motion criteria for boulder transport have historically been the primary methodology to infer hydrodynamics for inundation events in which other data do not exist. These methodologies apply drag, lift, gravitational, frictional, and sometimes inertial force or moment balances to determine minimum fluid velocities for boulders to slide, overturn, or lift from previously stationary positions. Many assumptions have been made to arrive at these relations: that boulders are shaped like rectangular prisms, that force coefficients are known to a sufficient degree of accuracy, and that initiation of motion leads to permanent motion and not just rocking in place (Weiss and Diplas, 2015). Of course, none of these assumptions are entirely true: still, some effects of these uncertainties may be investigated by varying parameters over plausible ranges, and by extending relations to include the effects of non-rectangular boulders. Once known, this degree of uncertainty in hydrodynamics feeds directly into incident wave or tsunami forcing, giving a better understanding of possible conditions leading to transport. Typhoon Haiyan provides a good opportunity to test relations, to see the range of conditions that may be possible, and to evaluate the plausibility of results.

3.1 Initiation of Motion for Non-Rectangular Boulders

The approach taken here follows closely the work of Nandasena et al. (2011), but without *a priori* assumptions of shape. For a non-rectangular-prismatic boulder with principal axis lengths (a,b,c), the volume will be $V = C_v abc$, where C_v is a dimensionless factor between 0 and 1. Likewise, the frontal area visible to flow perpendicular to long axis *a* will be $A_f = C_f ac$ and plan area for lift will be $A_p = C_p ab$, where both C_f and C_p are dimensionless factors between zero and 1. All factors $\left[C_v, C_f, C_p\right] = 1$ for a rectangular prism, but other values can be applied to any boulder shape as appropriate. The submerged weight is then $W = C_v\left(\rho_s - \rho_w\right) gabc$ where ρ_s is the rock density, ρ_w is the fluid density, and g is gravitational acceleration. On a slope of angle θ (positive uphill), the slope-perpendicular weight will be $F_{gz} = W\cos\theta$ and the

downslope component will be $F_{gx} = W \sin\theta$. When acted on by a fluid with velocity U parallel to the ground, the drag force will be $F_d = 0.5\rho_w C_d C_f acU^2$, where C_d is the drag coefficient, and the lift force will be $F_l = 0.5\rho_w C_l C_p abU^2$. Inertial forces are $F_I = C_m C_v \rho_w abc \frac{DU}{Dt}$, where C_m is the inertial coefficient. The frictional resistance to motion will be $F_f = \mu_s \left(F_{gz} - F_l \right)$, where μ_s is the coefficient of static friction. For incipient sliding motion, the force balance is then $F_d + F_I = F_f + F_{gx}$, which leads directly to:

$$U_{slide}^2 \geq \frac{2C_v c\left[\left(\rho_s / \rho_w - 1 \right) g \left(\mu_s \cos\theta + \sin\theta \right) - C_m \frac{DU}{Dt} \right]}{C_d C_f c / b + \mu_s C_l C_p} \quad (1)$$

For overturning motion, moments are summed about the boulder toe. For a boulder that is a rectangular prism, the gravitational restoring moment arm will be $b/2$. However, for a non-rectangular boulder (with corners and edges rounded or cut off), we take the pivot point as εb from the corner, which gives a slope-perpendicular restoring moment arm of $l_{gz} = b\left(1/2 - \varepsilon\right)$. The downslope component of weight will have a moment arm of l_{gx}: here we take this to remain unchanged from its rectangular value at $l_{gx} = c/2$, but it could differ with shape. Drag and inertial forces will have moment arms of l_d and l_I: here we both take as of $\left[l_d, l_I \right] = c/2$, while lift force will have a moment arm of l_l which we take here as $l_l = b\left(1/2 - \varepsilon\right)$. Frictional forces have a moment arm of zero. The moment balance about the toe for incipient overturning is then: $F_d l_d + F_l l_l + F_I l_I = F_{gx} l_{gx} + F_{gz} l_{gz}$. Simplification of this for assumed moment arms here yields:

$$U_{roll}^2 \geq \frac{2C_v c\left[\left(\rho_s / \rho_w - 1 \right) g \left(\cos\theta \left(1 - 2\varepsilon\right) + \sin\theta \frac{c}{b} \right) - C_m \frac{c}{b} \frac{DU}{Dt} \right]}{C_d C_f c^2 / b^2 + C_l C_p \left(1 - 2\varepsilon\right)} \quad (2)$$

For incipient lifting, the force balance is $F_{gz} = F_l$, which gives directly the relation used for joint-bounded computations:

$$U_{lift}^2 \geq \frac{2C_v\left(\rho_s/\rho_w - 1\right)gc\cos\theta}{C_l C_p} \quad (3)$$

The question now becomes how to define the unknown shape coefficients C_v, C_f, C_p, and ε, and moment arms. The best way to do this would be to measure detailed boulder shapes directly at field sites (e.g. Gienko et al., 2014; May et al., 2015); however, this was not accomplished here because of time and logistical concerns. Instead, we make simple analytical changes to the rectangular prism and cut off all edges and corners at distances $\varepsilon(a,b,c)$ as shown in Figure 14. This gives coefficients of $\left(C_v, C_f, C_p\right) = \left(1-6\varepsilon^2+\frac{16}{3}\varepsilon^3, 1-2\varepsilon^2, 1-2\varepsilon^2\right)$, governed by the single dimensionless parameter ε which also yields the overturning moment arm reduction in (2). If hydrodynamic parameters C_d and C_l are known, along with frictional coefficient μ_s, bed angle θ, and rock density ρ_s, minimum velocities to initiate different modes of motion may be computed. As the fraction of edges cut off, ε, approaches zero, equations (1-3) revert to the Nandasena et al. (2011) relations.

3.2 Inertial Forces and Scaling in Runup Bores

Inertial forces have proved problematic for incipient motion studies. Clearly, inertial forces (driven by accelerations) and drag forces (driven by velocities) will not be maximum at the same time. Additionally, acceleration in bore fronts may be maximum when the boulder is not fully immersed, making it difficult to apply standard coefficients. Finally, well-known inertial coefficients for free-stream flow are not the same as those for the wall-bounded flow found here (Dean and Dalrymple, 1991). Thus, the inclusion of inertial forces involves approximation and uncertainty. Still, if these uncertainties are quantified and evaluated, we may still obtain useful information.

For submerged boulders, inertial forces are usually ignored as unimportant in initiation of motion criteria (Nott, 2003; Nandasena et al.; 2011). For subaerial boulders, inertial forces are

sometimes included but given a small value (Nott, 2003), or omitted entirely (Nandasena et al., 2011). However, this is difficult to justify in a runup bore, where accelerations are certainly large: Jensen et al. (2003) showed accelerations exceeding 0.5g on a steep laboratory beach over much of the bore front, while Kennedy et al. (2016) computed swash zone inertial forces to be a significant fraction of drag forces, particularly for larger boulders where the relative importance of inertia is known to increase (Dean and Dalrymple, 1991). Dimensional Froude scaling suggests that, in a bore, $\frac{DU}{Dt} = C_g g$ (irrespective of scale!), with constant of proportionality C_g that will likely vary strongly with the detailed setting. In this case, maximum inertial forces may be written as

$$F_I = \rho_w C_m Vol \frac{DU}{Dt} = \rho_w C_m Vol C_g g = \rho_w g C_{1(-)} Vol \quad (4)$$

where $C_{1(-)}$ is a composite factor including inertial coefficients and acceleration. For drag forces, some significant simplifications may be established if we make a few assumptions about flow in the bore. If the boulder size at initiation of motion is roughly proportional to flow depth in the bore as would be expected from basic scaling, i.e. $(a,b,c) \propto (h+\eta)$, then boulder drag forces may be written as

$$F_d = 0.5 \rho_w C_d ac C_f \left(g\left(h+\eta\right)\right) Fr = \rho_w g C_{2(-)} Vol \quad (5)$$

where $C_{2(-)} = 0.5 C_d Fr \frac{Vol}{C_f ac\left(h+\eta\right)}$ is another composite factor that will depend on boulder shape among other factors. (We note that this assumption will not hold for strongly mobile boulders, whose dimensions will not scale with water depth.) Thus, it appears likely that both drag (4) and inertial (5) forces will have the same basic form for incipient motion in overland bores. Because of this, it is reasonable for relations such as (1-2) to combine drag and acceleration into one form: here for simplicity we will eliminate inertia and increase the mean value of drag coefficient to C_d =1.5 from drag-only value of C_d=1.05; however, there is very little guidance on how to do this. Finally, we note the assumption that bore depth at the boulder location, $h+\eta$, is proportional to boulder size also has strong implications in that, all other

411 things being equal, a boulder with doubled size will require double the inundation depth or local
412 wave height.

413

414 3.3 Coefficient Variation and Application to Haiyan

415 Although many studies have defined and used similar hydrodynamic and friction coefficients,
416 there is still substantial uncertainty about their values: since boulders are irregular, wall-bounded
417 and not free-stream, exist in finite water depths, and may be in environments with nearby flow
418 obstructions, standard laboratory values (e.g. Dean and Dalrymple, 1991) may not apply. Here,
419 we address this by treating all values as probabilistic and compute a Monte Carlo simulation of
420 the fluid velocities required for initiation of motion for boulders measured here. Random
421 realizations of parameters were generated as follows:

422
$$\begin{aligned} \varepsilon &= 0.28\left(0.6+0.8R_{\varepsilon}\right) \\ \mu_s &= 0.75\left(0.7+0.6R_{u}\right) \\ C_d &= 1.5\left(0.7+0.6R_{d}\right) \\ C_l &= 0.178\left(0.7+0.6R_{d}\right) \\ \rho_s &= 2500\left(0.95+0.1R_{\rho}\right)\text{kg/m}^3 \end{aligned} \tag{6}$$

423 where all $R_{(-)}$ are independent random variables with uniform probability distribution over the
424 range [0,1]. All dimensionless coefficient ranges are plausible based on judgement, while mean
425 densities of 2500kg/m^3 were measured from nine small samples of the native limestone.

426

427 As shown in Table 1, it was generally clear for the largest boulders measured here whether they
428 had been overturned during transport, moved through sliding only, or arose from joint-bounded
429 dislocation and transport. Thus, random simulations of parameters were used to estimate
430 incipient motion velocities for individual boulders using equations (1-3) as appropriate. Figure
431 15 shows means and standard deviations of velocities and masses for Monte Carlo simulations
432 with 10^4 random realizations for each boulder. Masses and velocities for rectangular prisms as
433 given by Nandasena et al. (2011) are also shown for comparison, using hydrodynamic
434 coefficients taken at the means of the ranges in (6).

Initial observations from Fig. 15 show that mean masses of the shaped boulders are strongly reduced from rectangular prism values, as would be expected. Mean stochastic masses for parameters employed here are 0.64 times those for rectangular prisms: other assumptions for the probability distribution of ε would of course provide different values. (We note that Engel and May (2012) and May et al. (2015) assumed masses were 0.6 times those for rectangular prisms as the result of detailed boulder measurements.) Additional detailed measurements of boulder shapes (Gienko et al., 2014), concentrating on parameters $\left(C_v, C_f, C_p, \varepsilon\right)$ and moment arms would clearly prove helpful to better define these values, but the ranges used here seem reasonable for now.

In addition to smaller masses, non-rectangular boulder shapes and probabilistic coefficients infer smaller incipient motion mean velocities for all transport modes. Sliding velocities differed slightly (~13% decrease), with lower submerged masses partially offset by lower frontal surface areas. Joint-bounded/lifting incipient velocities also decreased noticeably (~12%), although values for joint-bounded transport remain much higher than for other modes. The greatest decrease in computed incipient velocities arises in overturning transport. Here, largely due to the reduction of the gravitational moment arm, overturning velocities were by ~35% from rectangular prism values, which is a very large difference. Without these corrections, overturning velocities significantly exceeded those for sliding velocities, enough so that the differences in inferred velocities were somewhat problematic for boulders in the same areas. However, corrections for non-prismatic shape decrease overturning velocities enough that they are similar to sliding velocities. If the mean drag coefficient were decreased from 1.5 to 1.05 (as was assumed if drag and inertial forces were not combined), incipient velocities increase by ~15% (results not shown), so the uncertainty in inertial terms also adds significant uncertainty to inferred velocities.

Effects of uncertainties are significant: considering the largest moving blocks, ranges of inundation velocities for sliding and overturning are around 5-9m/s, with coefficient uncertainty

464 driving much of this range, and variations between individual boulders also important. All of
465 these values are reasonable for a storm such as Haiyan (Roeber and Bricker, 2015), and give an
466 estimate of the range of possible conditions on top of these low cliffs. However, the range is
467 large enough that the direct inference of wave heights would be problematic.

468

469 Stationary blocks, represented here with the velocities predicted to cause incipient sliding, have
470 plausible ranges of 6-9m/s, which possibly represents a (weak) division between moving and
471 stationary boulders. However, there is significant overlap so the division is not perfect. Still, the
472 presence of large stationary blocks does help to establish upper limits on velocities.

473

474 Relations to initiate joint-bounded transport using probabilistic relations with non-prismatic
475 boulders give mean fluid velocities of 18-22m/s for the two instances observed here, while
476 prismatic values are 22-23 m/s. All of these are much higher than inferred for other transport
477 modes. (We also note that an estimate of incipient transport velocity for joint-bounded boulder
478 ESA 5 in May et al. [2015] also greatly exceeds incipient velocity estimates for boulders with
479 other transport modes.) These inferred velocities for joint-bounded transport are not credible, and
480 yield local significant wave heights of around 40m using Nott's [2003] widely-used assumption
481 of a local Froude number of unity for storm waves, $H = U^2 / g$ with non-prismatic shapes and
482 stochastic coefficients. However, Nott's companion assumption that tsunamis have Froude
483 numbers of two gives inferred tsunami heights of 10m, which are more plausible for a coastline
484 directly facing the Philippine Trench subduction zone. Thus, without the direct confirmation of
485 transport during Haiyan, and with no coherent storm boulder ridges, standard methodology
486 would have incorrectly inferred a large, previously unknown, tsunami from observed motion of
487 these joint-bounded boulders.

488

489 Present results show clearly that simple joint-bounded transport theories do not work well here
490 for boulders on the immediate cliff edge. Velocities on the cliff face may be dominated by
491 vertical velocities with extremely high accelerations (Peregrine, 2003), and horizontal velocities
492 at the cliff edge have no real theories to fall back on. Cracks underneath the boulder, which must

493 exist to some degree prior to boulder transport, are another matter. High pressures on the cliff
494 face will propagate into these cracks, giving additional forces that do not arise from traditional
495 lift relations. Neither shallow water equations, which are often used to describe tsunami
496 evolution (Imamura et al., 2008), nor Boussinesq-type systems, which are often used to model
497 storm wave runup (Roeber and Bricker, 2015), will accurately simulate hydrodynamics for
498 vertical or near-vertical cliffs. Here, computational fluid dynamics (CFD) models or laboratory
499 experiments appear to be necessary to increase understanding in this very complex region. Until
500 then, however, results such as are found in Fig. 14 suggest that use of any incipient motion
501 relations at cliff edges to estimate incident wave heights is fraught with error, and should be
502 performed with very great caution.

503

504 **5. Conclusions**

505 Based on observations and analysis of boulder transport along a cliffed coastline during Super
506 Typhoon Haiyan, we conclude that:

507 • Typhoon Haiyan storm waves generated and transported isolated boulders, fields of
508 large boulders, and boulder/debris clusters (usually smaller boulders),
509 ○ Some large boulders observed here had originally been generated by one or
510 more earlier inundation events and transported further landward during
511 Haiyan,
512 • Runup along this cliffed coastline exceeded 15.2m above MSL during Typhoon
513 Haiyan, and extended at least 280m inland in some locations,
514 • Volumes and masses of many boulders moved by Haiyan strongly exceed the
515 literature-reported storm wave limits of 20m^3 and 20 tonnes, with measured values
516 here to 83m^3 and 209 tonnes,
517 ○ From present observations, and in conjunction with May et al. [2015],
518 Typhoon Haiyan has the largest clasts verified to have been transported by a
519 known storm,
520 • Boulder shapes that are not rectangular prisms tend to be transported more easily than
521 rectangular cross-sections, particularly for overturning motion,

- Joint-bounded boulder motion at cliff faces using initiation of motion criteria gives inferred velocities that are very different from other modes of motion, and should be used very cautiously,
- Global mass-elevation plots for storm-transported boulders in regions with extreme waves show a consistent upper envelope below which transport is observed and above which no transport observations exist.

6. Acknowledgements

This work was funded under NSF grants 1426445 and 1435007 (ABK), NSF GRFP 2013115239 (TT), and the Japan Society for the Promotion of Science Kakenhi grant (NM). Valerie Ambait, Nile April Robino, Catherine Ogatia Cueva, and Ariel Getiano provided significant logistical assistance to the field campaign. Discussions with Brian Atwater on an early draft helped to improve the paper.

7. References

Benner, R., T. Browne, H. Bruckner, D. Kelletat, and A. Scheffers (2010), Boulder transport by waves: progress in physical modelling, *Zeitschrift für Geomorphologie*, 54(S3), 127-146.

Bourgeois, J., and B. MacInnes (2010), Tsunami boulder transport and other dramatic effects of the 15 November 2006 central Kuril Islands tsunami on the island of Matua, *Zeitschrift für Geomorphologie*, 54(S3), 175-195.

Cox, R., Zentner, D.B., Kirchner, B.J., and M.S. Cook (2012), Boulder ridges on the Aran Islands (Ireland): Recent movements caused by storm waves, not tsunamis, *J. Geol.*, 120(3), 249-272.

Dean, R.G., and Darymple, R.A. (1991), *Water Wave Mechanics for Engineers and Scientists*, World Scientific, Singapore.

Engel, M., and S.M. May (2012), Bonaire's boulder fields revisited: evidence for Holocene tsunami impact on the Leeward Antilles, *Quaternary Science Reviews*, 54, 126-141.

549 Erdmann, W., Kelletat, D., Schaffers, A.M., and Haslett, S. (2015). *Origin and Formation of*
550 *Coastal Boulder Deposits at Galway Bay and the Aran Islands, Western Ireland*. Springer,
551 Heidelburg.

552 Fichaut, B., and S. Suanez (2011), Quarrying, transport, and deposition of cliff-top deposits
553 during extreme storm events: Banneg Island, Brittany, *Marine Geology*, **283**, 36-55.

554 Ford, D., and Williams, P. (2007), *Karst hydrogeology and geomorphology*, Wiley, Chichester.

555 Frohlich, C., M.J. Hornbach, F.W. Taylor, C.-C. Shen, A. Moala, A.E. Morton, and J. Kruger
556 (2009), Huge erratic boulders in Tonga deposited by a prehistoric tsunami, *Geology*, 37(2),
557 131-134.

558 Goto, K., M. Kunimasa, T. Kawana, J. Takahashi, and F. Imamura (2011), Emplacement and
559 movement of boulders by known storm waves – Field evidence from the Okinawa Islands,
560 Japan, *Marine Geology*, 283, 66-78.

561 Hansom, J.D., N.D.P. Bartrop, and A.M. Hall (2008). Modelling the processes of cliff-top
562 erosion and deposition under extreme storm waves, *Marine Geology*, 253, 36-50.

563 Hisamatsu, A., K. Goto, and F. Imamura (2014), Local paleo-tsunami size evaluation using
564 numerical modeling for boulder transport at Ishagaki Island, Japan, *Episodes*, 37(4), 265-276.

565 Imamura, F., Goto, K., and Ohkubo, S. (2008), A numerical model for the transport of a boulder
566 by a tsunami, *Journal of Geophysical Research – Oceans*, 113, C01008,
567 doi:10.1029/2007JC004170.

568 Jensen, A., Pedersen, G.K., and Wood, D.J. (2003), An experimental study of wave run-up at a
569 steep beach, *J. Fluid Mech*., 486, 161-188.

570 Joint Typhoon Warning Center (2013), Haiyan Best Track, retrieved from
571 http://www.usno.navy.mil/NOOC/nmfc-ph/RSS/jtwc/best_tracks/2013/2013s-
572 bwp/bwp312013.dat.

573 Kennedy, A.B., Mori, N., Zhang, Y., Yasuda, T., Chen, S.-E., Tajima, Y., Pecor, W., and Toride,
574 K. (2016), Observations and modeling of coastal boulder transport and loading during Super
575 Typhoon Haiyan, *Coastal Engineering Journal*, doi:10.1142/S0578563416400040.
576 Kelletat, D., Scheffers, A., and Scheffers, S. (2004), Holocene tsunami depositys on the
577 Bahaman Islands of Long Island and Eleuthera, *Zeitschrift für Geomorphologie*, 48(4), 519-
578 540.

579 Khan, S., E. Robinson, D.-A, Rowe, and R. Coutou (2010), Size and mass of shoreline boulders
580 moved and emplaced by recent hurricanes, Jamaica, *Zeitschrift für Geomorphologie*, 54(S3),
581 281-299.

582 Mas, E., Bricker, J., Kure, S., Adriano, B., Yi, C., Suppasri, A., and Koshimura, S. (2015), Field
583 survey report and satellite image interpretation of the 2013 Super Typhoon Haiyan in the
584 Philippines, *Natural Hazards and Earth System Sciences*, 15(4), 805-816.

585 May, S.M., Engel, M., Brill, D., Cuadra, C., Lagmay, A.M.F., Santiago, J., Suarez, J.K., Reyes,
586 M., and Brückner, H. (2015), Block and boulder transport in Eastern Samar (Philippines)
587 during Supertyphoon Haiyan, *Earth Surface Dynamics*, 3, 543-558.

588 Mcrfadgen, B.G., and Yaldwyn, J.C. (1984), Holocen sand dunes on Enderby Island, Auckland
589 Islands, *N.Z. J. Geology and Geophysics*, 27(1), 27-33.

590 Mori, N., M. Kato, S. Kim, H. Mase, Y. Shibutani, T. Takemi, K. Tsuboki, and T. Yasuda
591 (2014), Local amplification of storm surge by Super Typhoon Haiyan in Leyte Gulf,
592 *Geophys. Res. Lett.*, 41, doi:10.1002/2014GL060689.

593 Mylroie, J.E. (2008), Late Quaternary sea-level position: evidence from Bahamian carbonate
594 deposition and dissolution cycles, *Quaternary International*, 183, 61-75.

595 Nandasena, N.A.K., R. Paris, and N. Tanaka (2011), Reassessment of hydrodynamic equations:
596 Minimum flow velocity to initiate boulder transport by high energy events (storms,
597 tsunamis), *Marine Geology*, 281, 70-84.

598 Nandasena, N.A.K., Tanaka, N., Sasaki, Y., and M. Oda (2013), Boulder transport by the 2011
599 Great East Japan tsunami: Comprehensive field observations and whither model predictions?
600 *Marine Geology*, 346, 292-309.

National Disaster Risk Reduction and Management Council (2014), NDRRMC update: SitRep No. 108 Effects of Typhoon "YOLANDA" (HAIYAN), Retrieved May 29, 2015.

Nott, J. (2003), Waves, coastal boulder deposits and the importance of the pre-transport setting, *Earth and Planetary Science Letters*, 210, 269-276.

Paris, R., P. Wassmer, J. Sartohadi, F. Lavigne, B. Barthomeuf, E. Desgages, D. Grancher, P. Baumert, F. Vautier, D. Brunstein, and C. Gomez (2009), Tsunamis as geomorphic crises: lessons from the December 26, 2004 tsunami in Lhok Nga, West Banda Aceh (Sumatra, Indonesia), *Geomorphology*, 104, 59-72.

Paris, R., Naylor, L.A., and W.J. Stephenson (2011), Boulders as a signature of storms on rock coasts, *Marine Geology*, 283, 1-11.

Peregrine, D.H. (2003), Water-wave impact on walls, *Ann. Rev. Fluid Mech.*, 35, 23-43.

Ramalho, R.S., Winckler. G., Madeira, G., Helffrich, G.R., Hipólito, A., Quartau, R., Adena, K., and J.M. Schaefer (2015). Hazard potential of volcanic flank collapses raised by new megatsunami evidence, *Science Advances*, doi:10.1126/sciadv.1500456.

Roeber, V., and J.D. Bricker (2015), Destructive tsunami-like wave generated by surf beat over a coral reef during Typhoon Haiyan, *Nature Communications*, 6, 7854, doi:10.1038/ncomms8854.

Scheffers, A., Scheffers, S., and D. Kelletat (2005), Paleo-tsunami relics on the southern and central Antillean island arc, *Journal of Coastal Research*, 21(2), 263-273.

Scheffers, A., and S. Kinis (2014), Stable imbrication and delicate/unstable settings in coastal boulder deposits: indicators for tsunami dislocation? *Quaternary International*, 332, 73-84.

Shah-hosseini, M., Morhange, C., Beni, A.N., Marriner, N., Lahijani, H., Hamzeh, M., and Sabatier, F. (2011), Coastal boulders as evidence for high-energy waves on the Iranian coast of Makran, Marine Geology, 290, 17-28.

Shimozono, T., Y. Tajima, A.B. Kennedy, H. Nobuoko, J. Sasaki, and S. Sato (2015), Combined infragravity wave and sea-swell runup over fringing reefs by super typhoon Haiyan, *J. Geophys. Res.-Oceans*, doi:10.1002/2015JC010760.

628 Taborosi, D., and Kazmer, M. (2013), Erosional and Depositional Textures and Structures in
629 Coastal Karst Landscapes, Coastal Research Library, Vol 5., 15-57.

630 Tajima, Y., T. Yasuda, B.M. Pacheco, E.C. Cruz, K. Kawasaki, H. Nobuoka, M. Miyamoto, Y.
631 Asano, Y., T. Arikawa, N. Ortigas, R. Aquino, W. Mata, J. Valdez, and F. Briones (2014),
632 Initial report of JSCE-PICE joint survey on the storm surge disaster caused by Typhoon
633 Haiyan, *Coastal Engineering Journal*, 56, 1450006.

634 Watt. S.E., Jaffe, B.E., Morton, R.A., Richmond, B.M., and G. Gelfenbaum (2010). *Description*
635 *of extreme-wave deposits on the northern coast of Bonaire, Netherlands, Antilles*, Open-File
636 Report 2010-1180, U.S. Geological Survey, Reston, Virginia.

637 Williams, D.M., and Hall, A.M. (2004), Cliff-top megaclast deposits of Ireland, a record of
638 extreme waves in the North Atlantic – storms or tsunamis? *Marine Geology*, 206, 101-117.

639

640 Table 1. Characteristics of measured boulders with a-axis greater than 5m. Boulders marked by * could not be reached with RTK
641 GPS, and their elevations are estimates only.

ID	Latitude	Longitude	a (m)	b (m)	c (m)	Ground Elev (m)	Top Elev (m)	x (m)	Δx (m)	Vol (m^3)	Mass (t)	Observed Motion
South Region												
B53-3	10.999316	125.798082	5.2	3.6	1.85	11.6	13.3	108		20.8	52	Overturning
999	11.000487	125.798321	7.3	5.1	3.2	11.1	14.3	30	30	71.5	179	Joint Bounded
B3	11.001121	125.797323	7.2	5.0	2.7	9.9	13.0	124		58.3	146	Overturning
B108	11.005203	125.794453	6.9	3.3	2.55	8.8	11.9	109		34.8	87	Overturning
A003	11.005234	125.794300	6.2	3.6	2.68	7.5	10.3	97		35.9	90	Sliding
S1	11.004425	125.795566	7.4	3.26	2.3	7.9	11.1	59		33.3	82	Sliding
1122-A	11.004196	125.795224	5.1	2.5	2.3		12.8	104		17.6	44	Overturning
B70	11.002839	125.796205	6.1	5.4	2.8	11.3	13.5	102		55.3	138	Sliding
B71	11.002965	125.796038	5.9	3.7	2.9	11.5	14.2	106		38.0	95	Overturning
North Region												
N0	11.014232	125.786753	5.9	3.1	2.8		15.2	65	12	30.7	77	Sliding
N1	11.012470	125.786755	6.1	3.0	2.6	7.8	10.1	65	45-60	28.6	71	Sliding
N2	11.010163	125.789890	7.45	4.9	3.1	7.3	10.4	27	21	67.9	170	Joint Bounded
B343*	11.023268	125.780017	7.7	5.5	2.3	5-9		92		58.4	146	Overturning
B358*	11.023597	125.780120	5.95	3.5	2.0	5-9		56		25.0	62	Sliding
B345*	11.022797	125.780442	7.7	5.3	3.4	5-9		105		83.3	208	Sliding
B320	11.020260	125.782330	7.3	5.6	3.4	7.00	9.7	130		83.4	208	Sliding
B321	11.020365	125.782259	7.4	4.5	2.8	6.4	8.7	127		55.9	140	Sliding
B342a	11.021368	125.780824	5.3	2.9	1.8	7.6	9.5	168		16.6	41	Sliding
B327	11.021267	125.781356	6.3	4.4	2.4	6.5	9.1	132		39.9	100	Overturning
B327b	11.021278	125.781199	6.0	3.9	3.4	6.6	9.4	144		47.7	119	Overturning
No Motion												
B122	11.003293	125.796156	7.5	6.5	4.5	9.2	11.5	82	0	131.6	329	No Motion
B311	11.019267	125.783896	8.0	5.0	2.7		12.6	69	0	64.8	162	No Motion

642

643 **Figures**

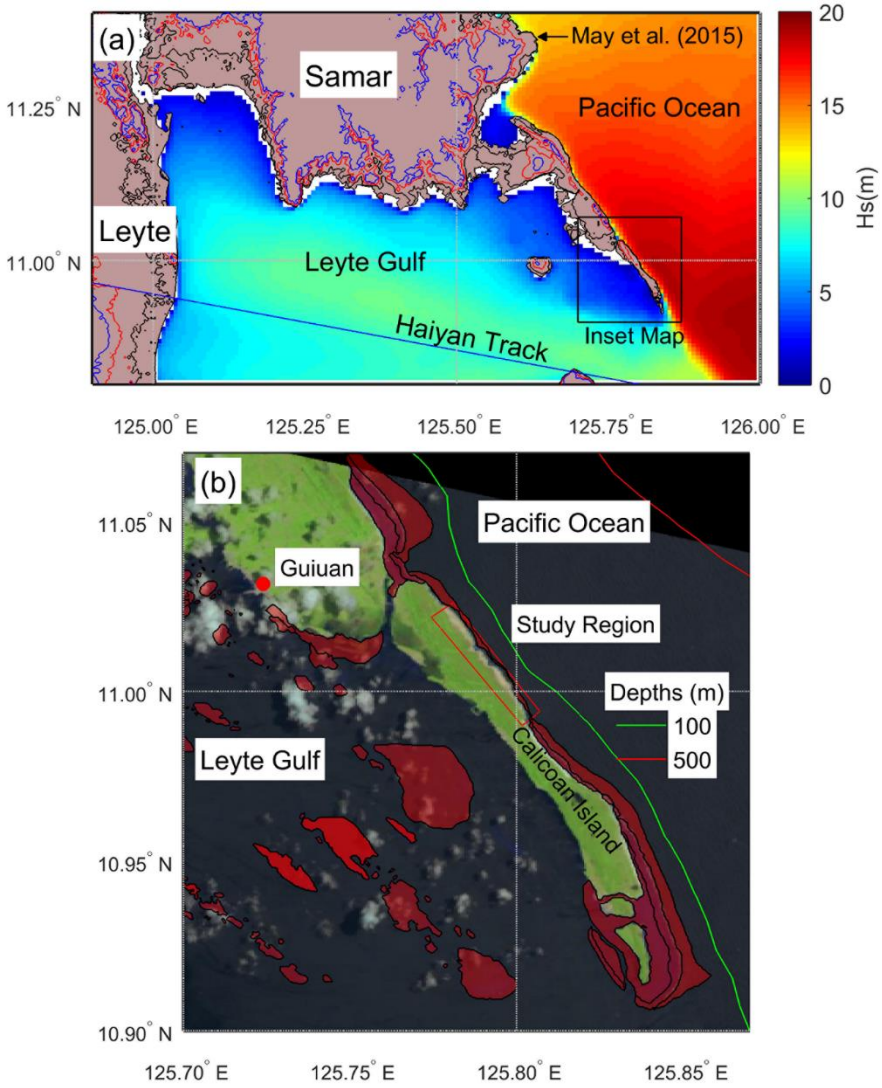

644

645 Figure 1. Typhoon Haiyan and study region on Calicoan Island. (a) Overview map showing
646 Haiyan Track, (10,50,100) meter elevation contours, and hindcast wave heights; (b) Inset map of
647 study region on Calicoan Island, depth contours, and coral reef locations in red. Background
648 image from Landsat May 2, 2014.

649

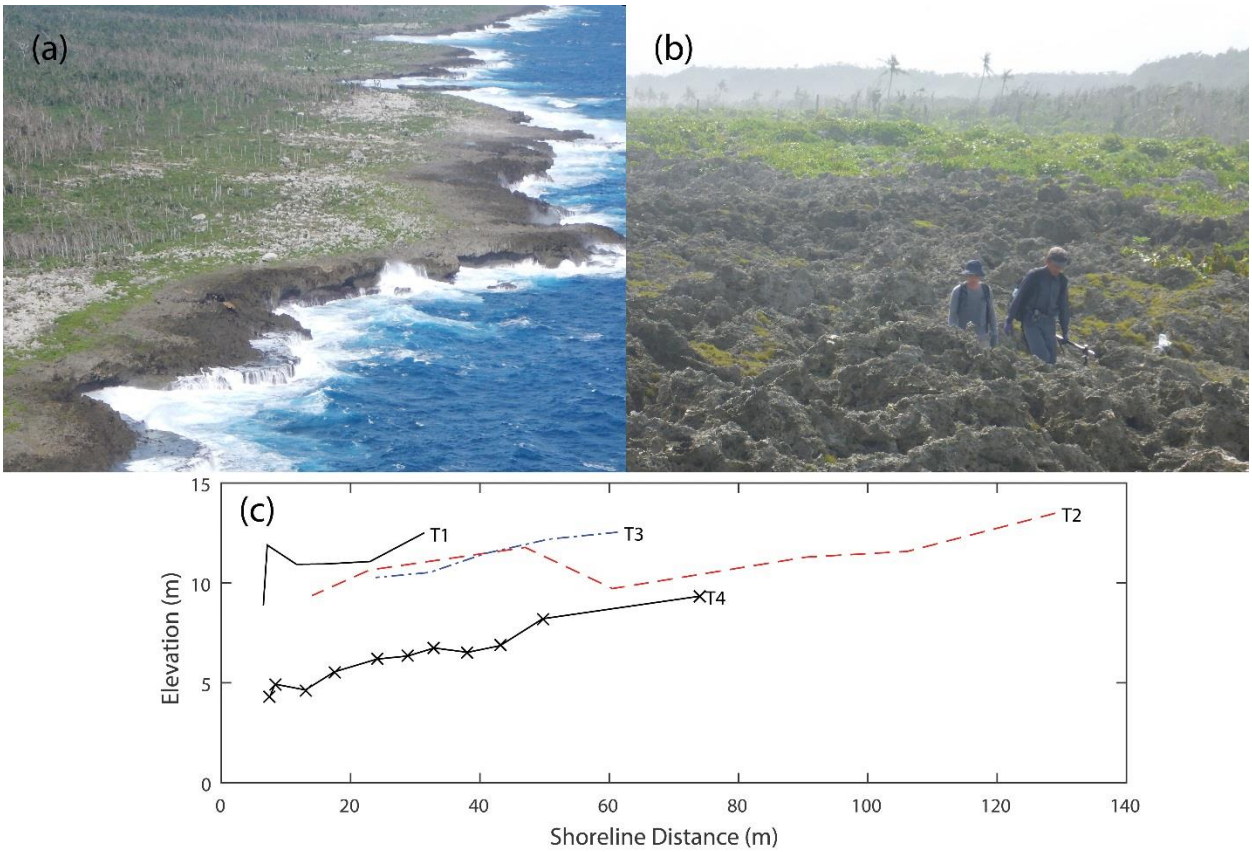

Figure 2. (a) Aerial view of a portion of the study region, facing northwest; (b) Rough phytokarst topography in the sea-spray region; (c) Partial elevation transects. Locations are shown in Figure 5.

Figure 3. Example of low elevation blocks and boulders in pocket beach that were not measured. Location is shown in Fig. 5.

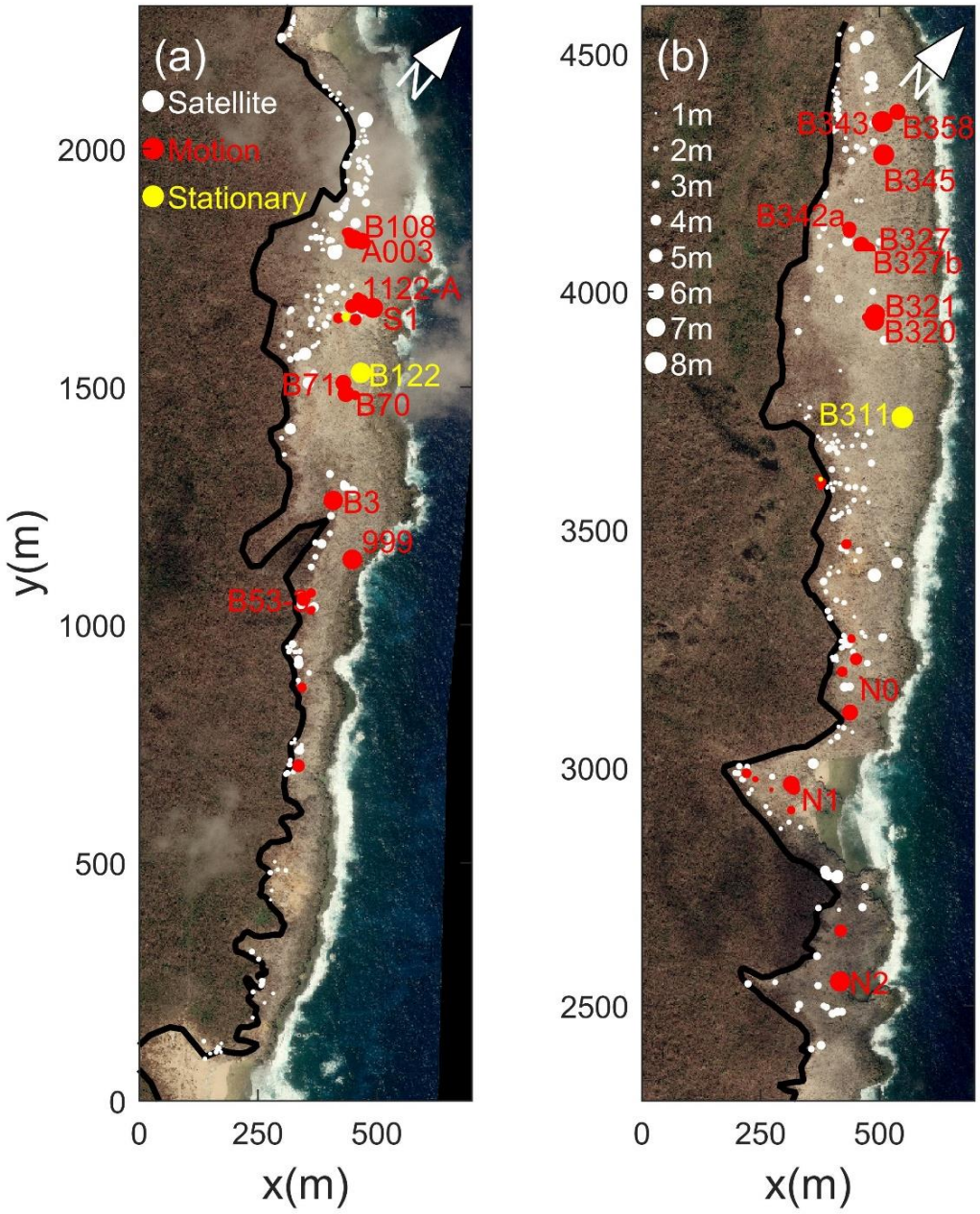

Figure 4. Runup inland extent (black line), boulder locations (●) (white symbols: satellite observations; red: ground observations of transported boulders; yellow: ground observations of stationary boulders); length of a-axis. (a) y=0-2300m alongshore coordinate (south region of study area); (b) y=2300-4600m (north region). Background image taken December 15, 2013 from Pleiades 1B satellite.

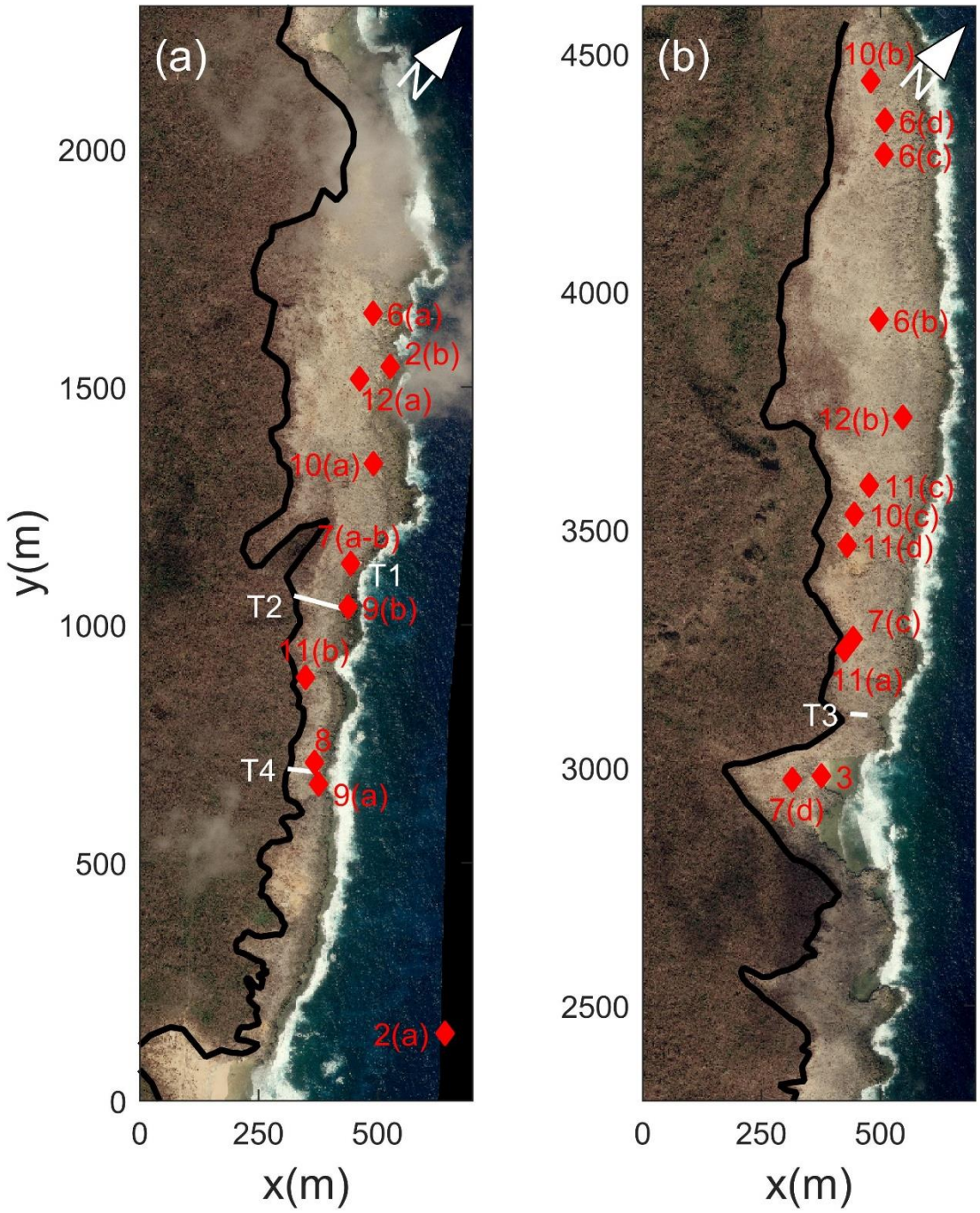

667

668 Figure 5. Locations of Figures referenced in this paper. (a) y=0-2300m alongshore coordinate
669 (south region of study area); (b) y=2300-4600m (north region). Background image taken
670 December 15, 2013 from Pleiades 1B satellite.

671

672

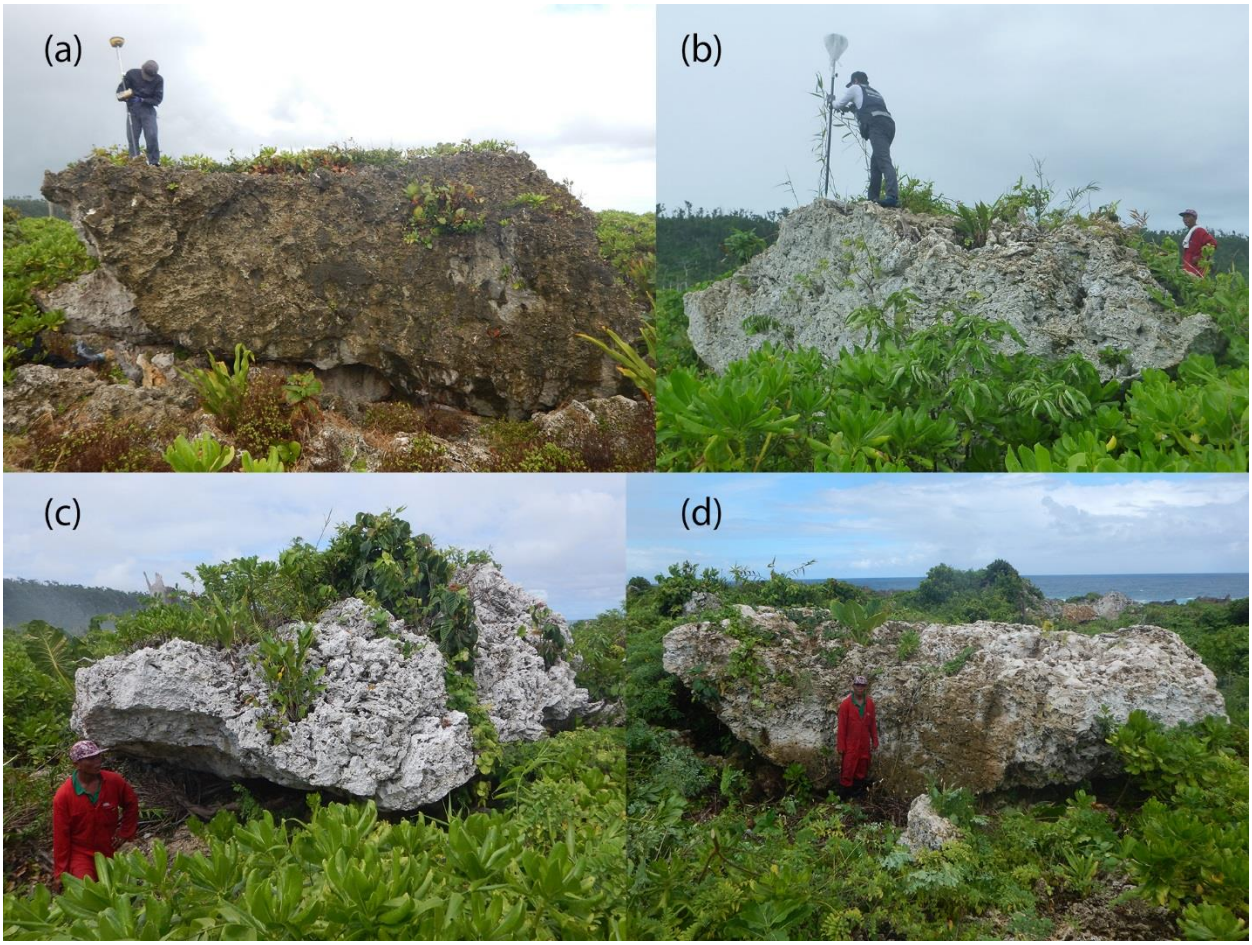

673
674 Figure 6. Examples of large boulders transported by Typhoon Haiyan waves. (a) S1; (b) B320;
675 (c) B345; (d) B343. Additional photos and settings for all large boulders are given in
676 Supplemental Figures S.1.1-S.1.15. Locations are shown in Figures 4-5.

677

678

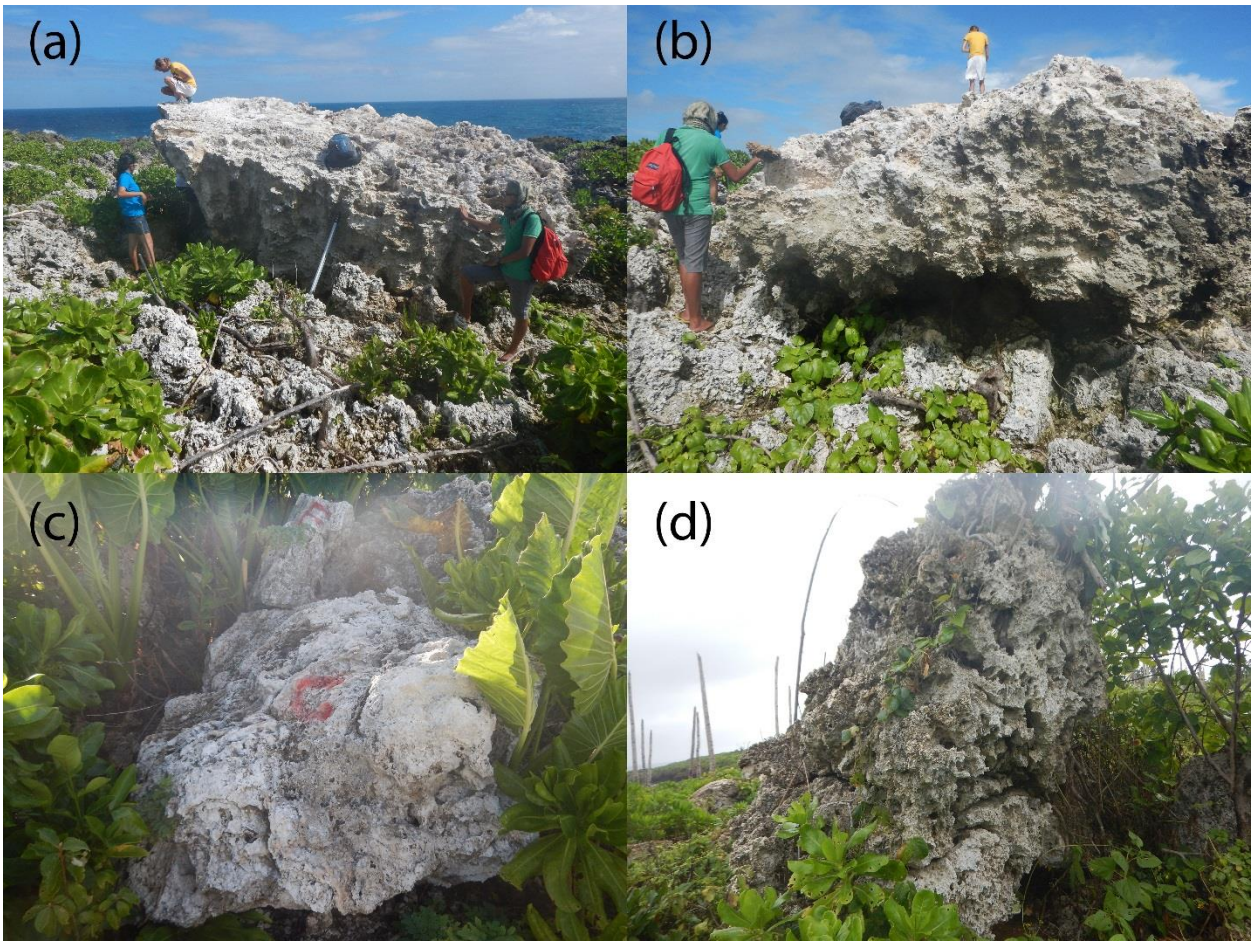

679

680 Figure 7. Weathering and angularity differences across observed boulders. (a-b) Front and back
681 sides of Boulder 999, showing more exposed (rough gray), and protected (smoother white) pre-
682 storm surfaces; (c) pre-storm underside of overturned boulder showing smooth, white
683 depositional karst features; (d) Very angular transported boulder whose dark gray left side was
684 directly exposed to sea spray pre-storm. Locations are shown in Fig. 5.

685

686

687

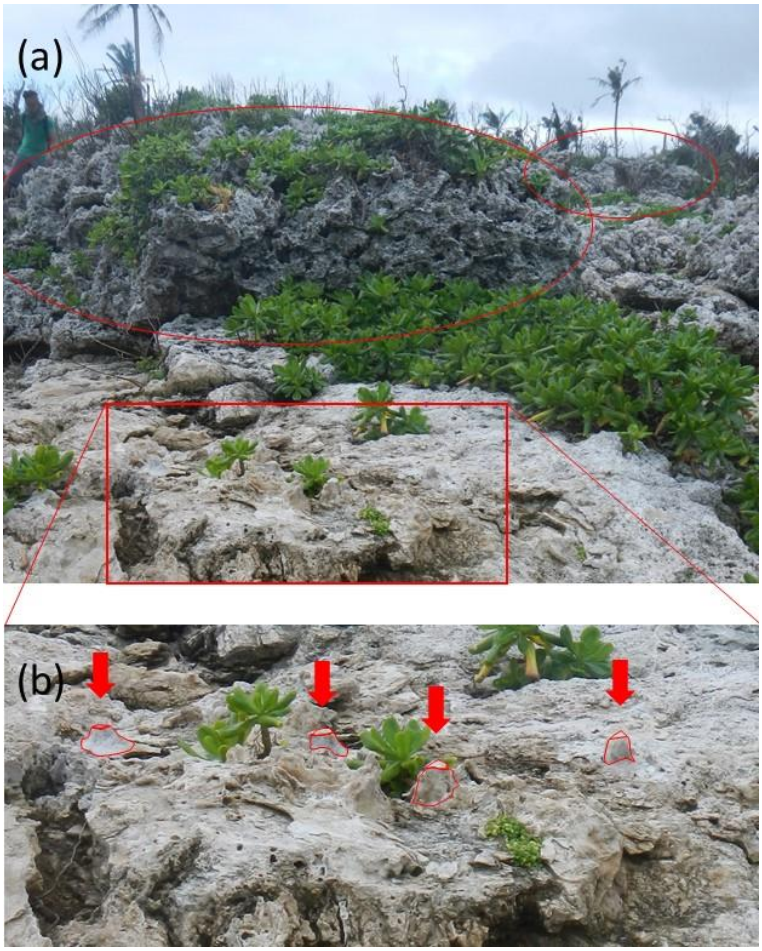

688

689 Figure 8. Karst features generated underneath boulders that were transported during Haiyan. (a)
690 Transported boulders (circled), and overall setting; (b) Inset of bedrock with arrows showing
691 karst solution columns that were attached to boulder undersides pre-storm. Location is shown in
692 Fig. 5.

693

694

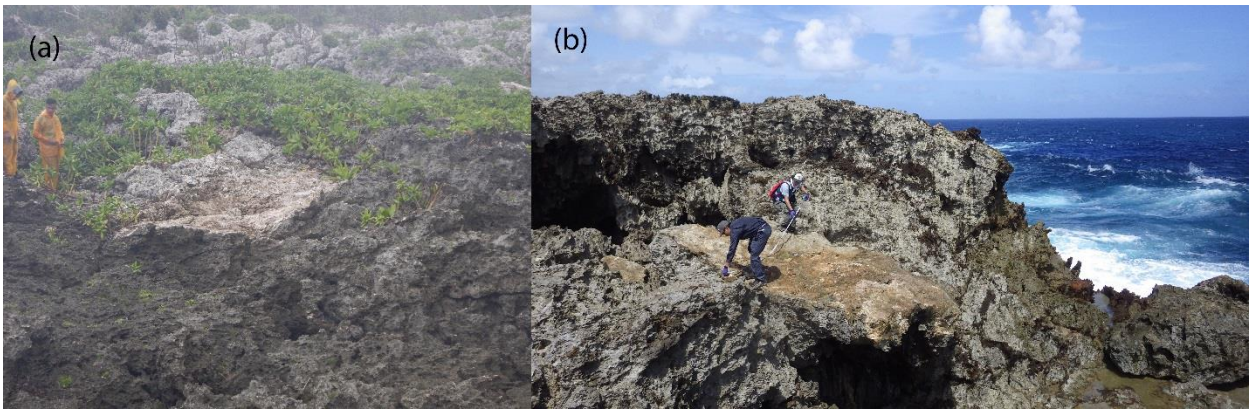

Figure 9. Typical whitish to brownish clifftop scars from rock breakage and transport during Haiyan. Locations are shown in Figure 5.

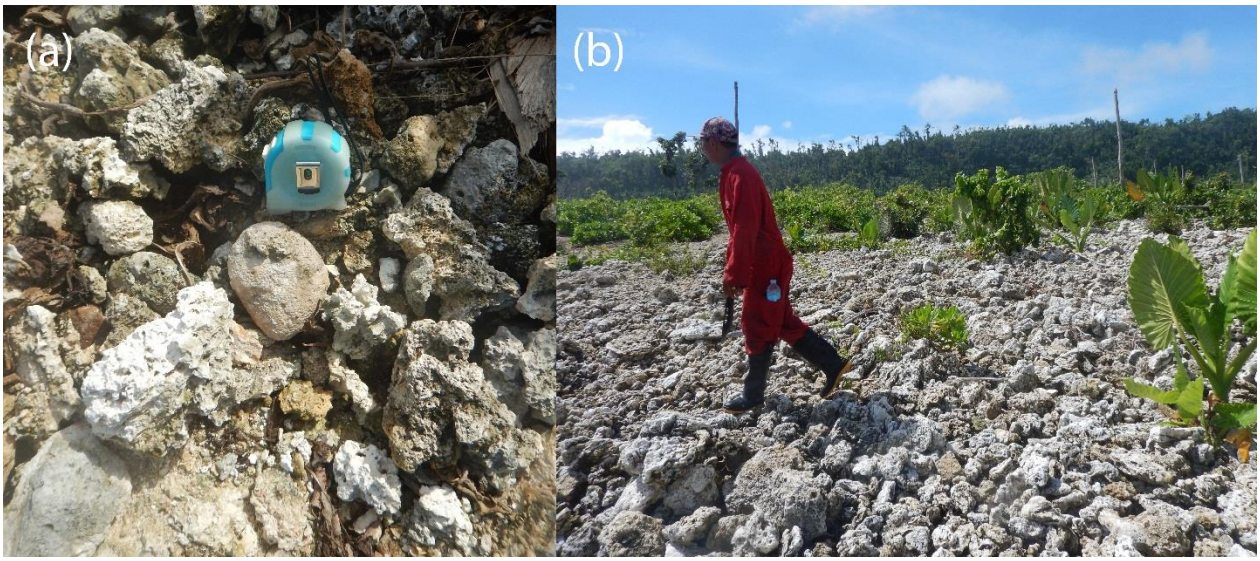

699

700 Figure 10. Inland beaches from Haiyan runup. (a) Cobble beach, showing relatively rare clast of
701 subaqueous origin (rounded) surrounded by very angular to angular subaerially-generated clasts;
702 (b) Boulder/cobble beach approximately 100 m inland. Locations are shown in Figure 5.

703

704

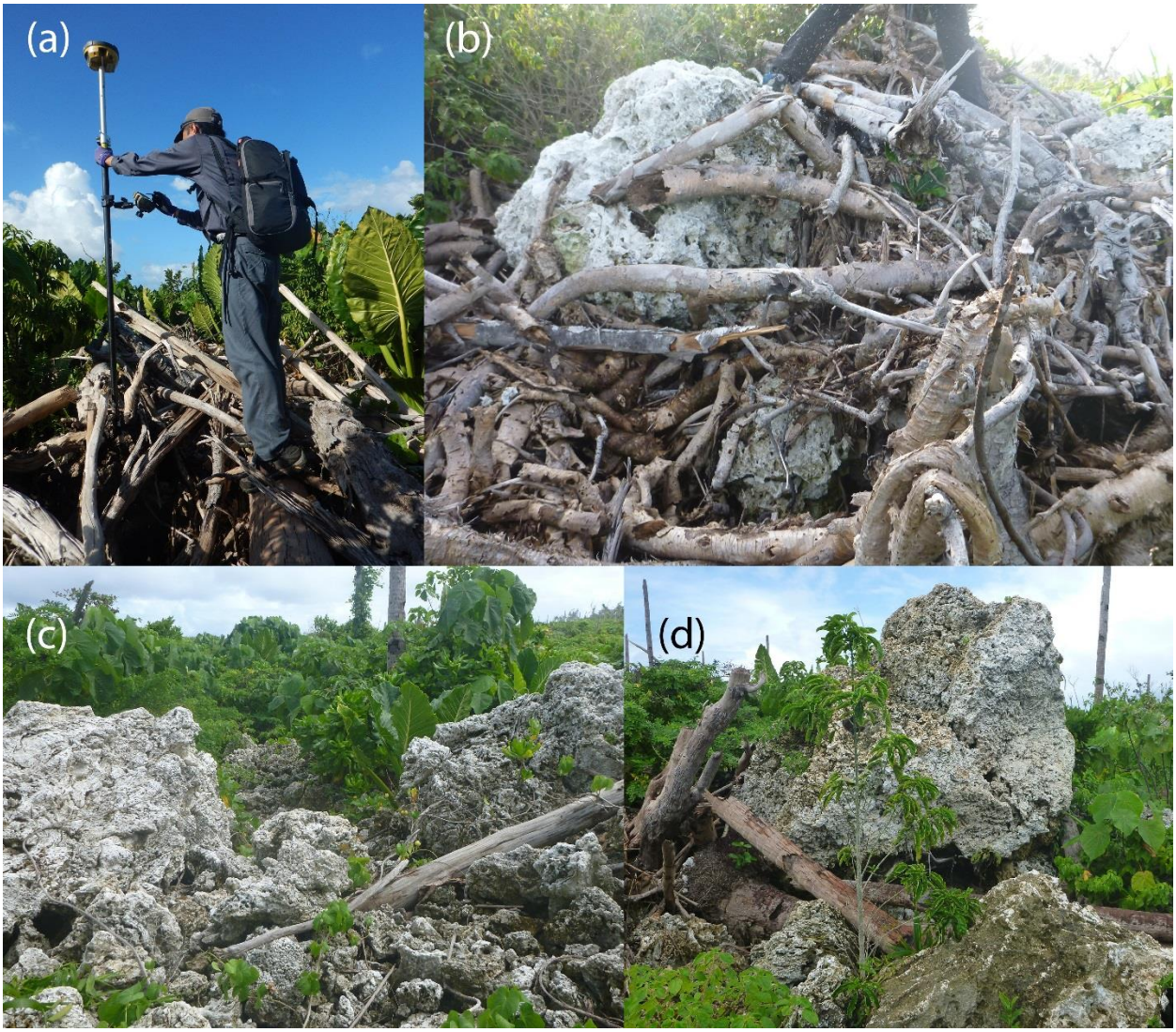

705

706 Figure 11. Debris clusters generated by Haiyan runup. (a) Vegetative debris (mostly trees and
707 woody shrubs); (b) Mixed boulder/vegetative debris; (c-d) Mostly rocky debris clusters.
708 Locations are shown in Figure 5.

709

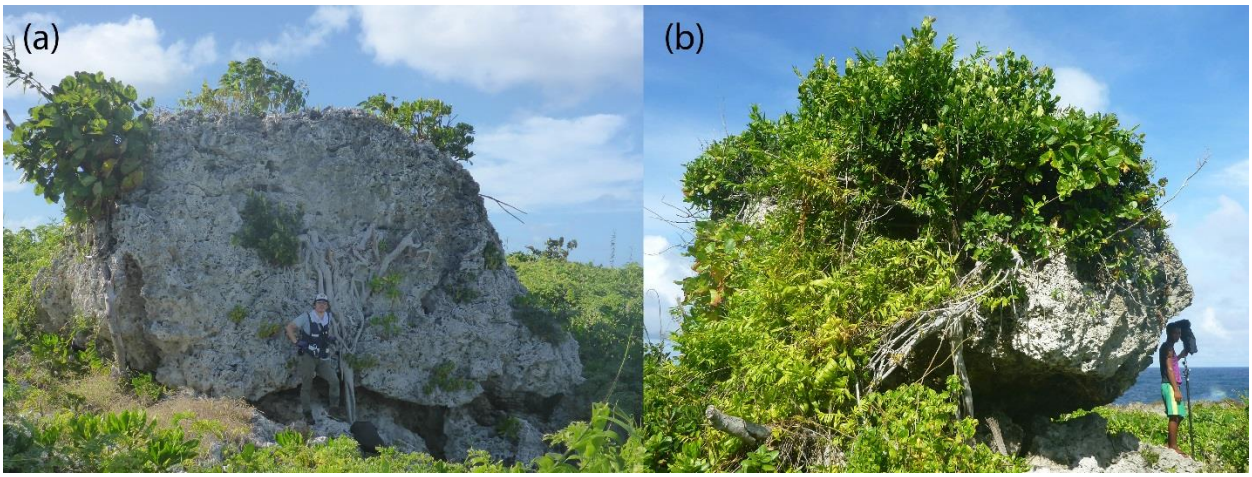

Figure 12. Large blocks that did not move during Haiyan. (a) B122; (b) B311. Locations are shown in Figs. 4-5, and aerial photographs are in supplemental Figs S.2.1-S.2.2.

715

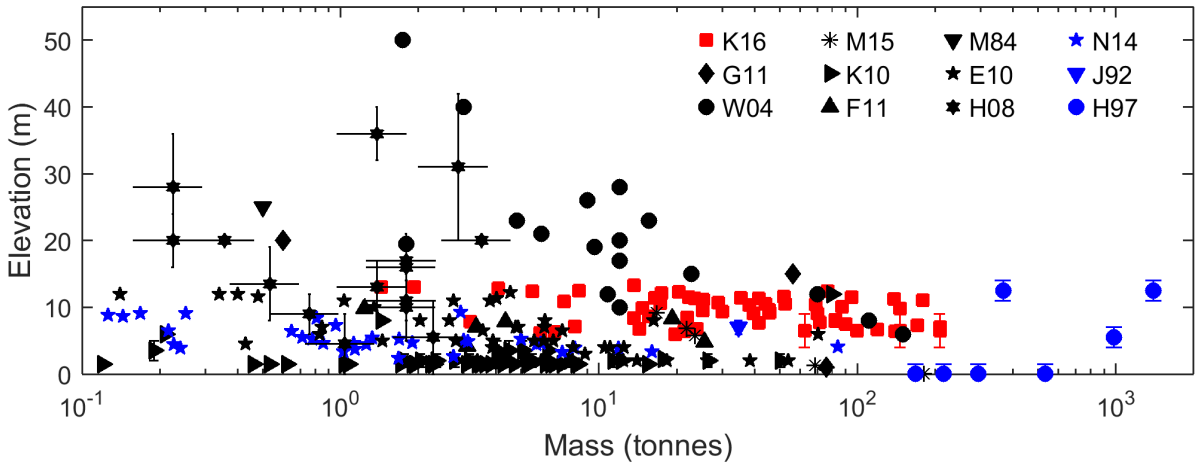

716

717 Figure 13. Masses of coastal boulders transported by known storm waves as a function of
718 ground elevation: (■) Present study; (♦) Okinawan Islands, Goto et al. (2011); (●) Aran Islands,
719 Ireland, Williams and Hall (2004); (*) Typhoon Haiyan, May et al. (2015); (►) Jamaica, Khan
720 et al. (2010); (▲) Banneg Island, France, Fichaut and Suanez (2011); (▼) Enderby Island,
721 McFadgen and Yalwyn (1984); (pentagram) Iceland, Etienne and Paris (2010); (hexagram+error
722 bars) Scotland, Hansom et al. (2008). Boulders with indeterminate or disputed origins:
723 (pentagram) Lanyu Island, Taiwan, Nakamura et al. (2014); (▼) Grand Cayman Island, Jones
724 and Hunter (1992); (●) Eleuthera Island, Bahamas, Hearty (1997).

725

726

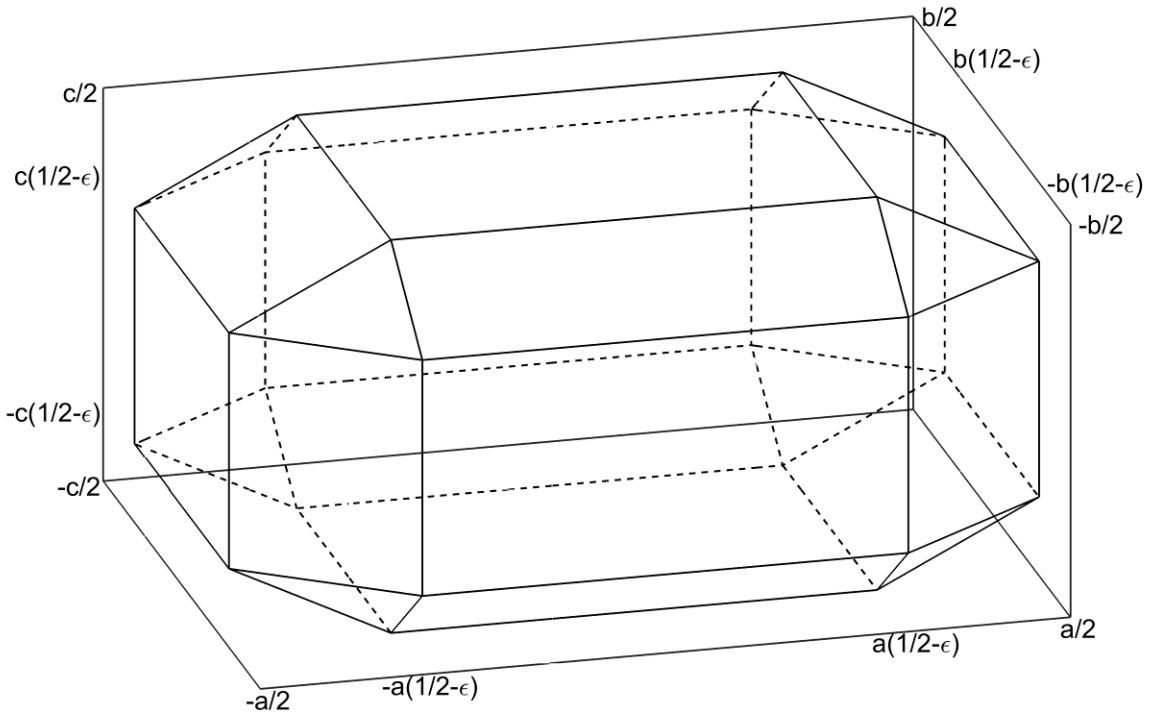

727

728 Figure 14. Definition sketch for reduced boulders, with hidden edges shown as dashed lines.

729

730

731

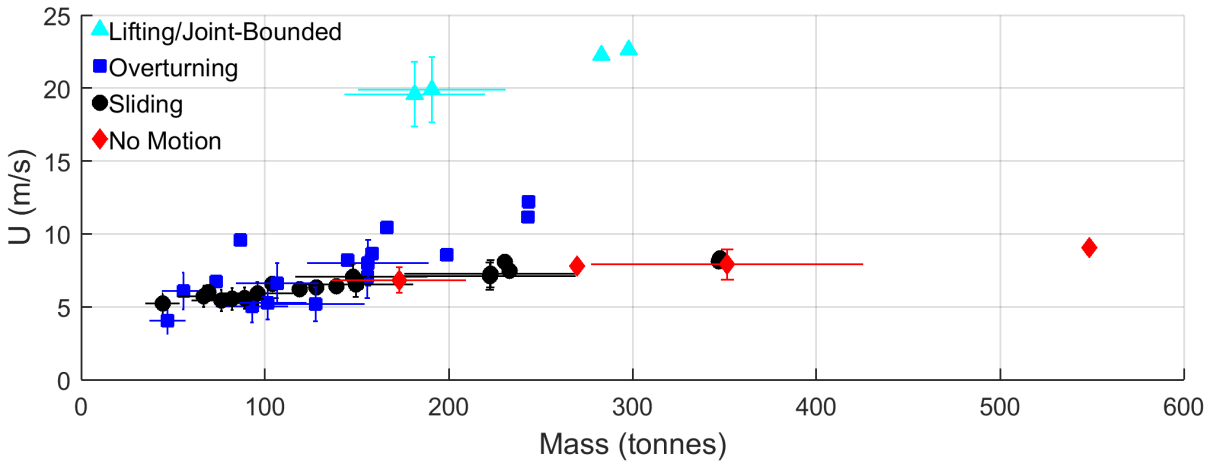

732

733 Figure 15. Probabilistic inferred initiation of motion fluid velocities for large boulders measured
734 here using Equations (1-3,6), showing 1-sigma error bars. Symbols without error bars show
735 deterministic relations of Nandasena et al. (2011) for rectangular prisms.

736

737